





Effect of non- α -cluster projectile on incomplete-fusion dynamics: Experimental study of the $^{14}\text{N} + ^{181}\text{Ta}$ system

M. Shariq Asnain ^{1,*}, Mohd. Shuaib ¹, Ishfaq Majeed,¹ Manoj Kumar Sharma,² Vijay R. Sharma ³, Abhishek Yadav,⁴ Devendra P. Singh,⁵ Pushpendra P. Singh,⁶ Unnati Gupta,⁷ Rudra N. Sahoo,⁶ Arshiya Sood,⁶ Malika Kaushik,⁶ Sushil Kumar,⁸ R. Kumar,⁸ B. P. Singh,^{1,†} and R. Prasad ¹

¹Accelerator Laboratory, Department of Physics, A. M. U, Aligarh-202 002, Uttar Pradesh, India

²Department of Physics, Shri Varshney College, Aligarh-202 001, Uttar Pradesh, India

³Instituto de Fisica, Universidad Nacional Autonoma de Mexico, Mexico City 04510, Mexico

⁴Department of Physics, Faculty of Natural Sciences, Jamia Millia Islamia, New Delhi-110025, India

⁵Department of Physics, University of Petroleum and Energy Studies, Dehradun-248 007, Uttarakhand, India

⁶Department of Physics, Indian Institute of Technology, Ropar-140 001, Punjab, India

⁷Amity Institute of Nuclear Science and Technology, Amity University, Noida-201313, Uttar Pradesh, India

⁸Inter University Accelerator Centre, Aruna Asaf Ali Marg, New Delhi-110067, India



(Received 15 June 2021; accepted 1 September 2021; published 14 September 2021)

In order to study incomplete fusion (ICF) reaction dynamics, the present work manifests the role of a non- α -cluster ^{14}N projectile on ^{181}Ta target at energies $\approx 4\text{--}7$ MeV/nucleon using the offline γ -ray spectroscopy. The excitation functions for 15 reaction residues populated in $^{14}\text{N} + ^{181}\text{Ta}$ system have been measured and analyzed within the framework of statistical model code PACE4. The experimentally measured excitation functions of evaporation residues populated via xn/pxn channels are found to be well reproduced by the predictions of code PACE4, which confirms their production solely via complete fusion process. However, an enhancement in the measured excitation function as compared to PACE4 calculations, particularly in tail portion of ^{192}Hg residue ($3n$ channel) has been observed indicating the presence of precompound emission. A significant contribution from precursor decay in pxn channels has also been observed. An enhancement in the measured excitation functions for α -emitting channels as compared to the PACE4 predictions has been observed and attributed to the incomplete fusion process. Further, the contribution from incomplete fusion process in the $^{14}\text{N} + ^{181}\text{Ta}$ system has also been deduced in terms of strength function (F_{ICF}). The results have been discussed in terms of the parameters which influence the dynamics of ICF process. The F_{ICF} is found to depend strongly on projectile energies, the product of projectile and target charges, and α - Q value of the projectile.

DOI: [10.1103/PhysRevC.104.034616](https://doi.org/10.1103/PhysRevC.104.034616)

I. INTRODUCTION

The study of heavy-ion (HI) fusion reactions has been extensively used to get information about the nuclear structure and also to study the possibility of producing superheavy elements (SHE) [1–5]. However, due to the presence of break-up/incomplete fusion (ICF) reactions, complexity may arise to synthesize the SHE [6–10]. Recent studies of HI interactions emphasized the presence of ICF reactions along with the complete fusion (CF) reactions even at energies $\approx 4\text{--}7$ MeV/nucleon [9, 11, 12]. Therefore, a proper understanding of ICF reaction dynamics is adequately required to derive information about nuclear reaction dynamics. In case of CF, the entire projectile with partial waves $\ell < \ell_{\text{crit}}$ is captured by the target nucleus to form a highly excited composite system known as compound nucleus (CN). On the other hand, the ICF process involves higher values of ℓ ($\ell > \ell_{\text{crit}}$). At these values

of ℓ , the attractive fusion pocket in the potential energy curve disappears, as a result the entire fusion of the projectile with the target nucleus is hindered. In order to provide sustainable input angular momentum (ℓ) required for fusion, the projectile breaks-up into its fragment(s) and one of the fragments fuses with the target nucleus, whereas the remnant continues to move in the forward direction without any interaction. A typical representation of CF and ICF processes for the system $^{14}\text{N} + ^{181}\text{Ta}$ is shown in Figs. 1(a) and 1(b), respectively. As may be seen from these figures, the composite system ($^{191}\text{Pt}^*$) formed in case of ICF has less charge, mass, and excitation energy as compared to the composite system ($^{195}\text{Hg}^*$) formed due to CF process.

The first experimental evidence of ICF process in HI interactions was reported by Britt and Quinton [13]. They measured angular distribution, energy spectra, and absolute cross section for α particles emitted using α -cluster beams ^{12}C and ^{16}O and also a non- α -cluster beam ^{14}N on the targets ^{197}Au and ^{209}Bi [13]. Their results indicated that direct α particles came primarily from the break-up of incident projectile in grazing collisions. However, they did not separate out

*asnainshariq@gmail.com

†bpsinghamu@gmail.com

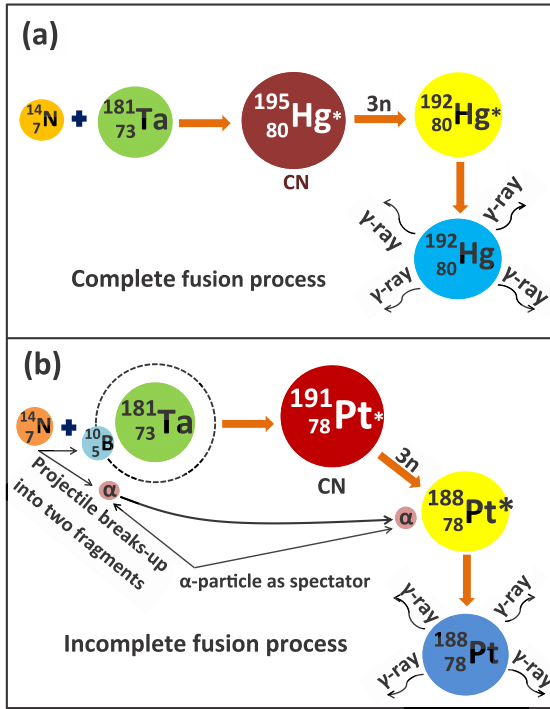


FIG. 1. A pictorial representation of (a) CF and (b) ICF process.

the contributions of direct α and evaporated α emitted in the collision. The advancement in the study of ICF reactions got a boost after the γ -ray coincidence experiments were performed by Inamura *et al.* [14]. In these experiments it was found that direct α -particle emitting reactions involved relatively higher values of angular momenta (ℓ), resulting in the population of high spin states of the residual nuclei. The angular distribution and gamma multiplicity experiments done by Geoffrey [15] provided the origin of PLFs, viz., ^4He , ^8Be , and ^{12}C in the peripheral collisions of an α -cluster beam ^{16}O with ^{154}Sm target nuclei. Gerschel [16] found that a wider range of ℓ values above the ℓ_{crit} are required for fusion with deformed target as compared to spherical target nuclei. The measurements of spin distribution of reaction residues suggested the involvement of higher angular momentum with the ICF process as compared to CF process [17–19]. In order to understand the dynamics of ICF process, various theoretical models, viz., the break-up fusion model [20,21], the sum-rule model [22], the exciton model [23], the promptly emitted particles model [24], etc., have been proposed. It has been observed that the above-mentioned models satisfactorily explain the ICF data at energies ≥ 10 MeV/nucleon but they are unable to explain it completely at lower energies (≈ 4 –7 MeV/nucleon). Hence, due to the unavailability of any reliable theoretical model at low energies, the ICF reaction dynamics is still not well explored. Further, the strength of ICF reactions and its correlations with various entrance channel parameters have been reported mostly for α -cluster beams, viz., ^{12}C and ^{16}O on various targets [9,25–29]. However, the studies using non- α -cluster beams like ^{13}C , ^{14}N , ^{18}O , and ^{19}F on various targets are scarce [11,30].

The aim of the present work is to explore the role of a non- α -cluster beam ^{14}N on ICF reaction dynamics and how does it correlate with α -cluster beams at low energies. Keeping this in mind, the experiments have been carried out to measure the excitation functions (EFs) of several reaction residues populated via CF and/or ICF processes in $^{14}\text{N} + ^{181}\text{Ta}$ system at energies ≈ 4 –7 MeV/nucleon. It may be pointed out that ^{14}N is a non- α -cluster beam. The experimentally measured EFs of reaction residues have been analyzed within the framework of statistical model code PACE4 [31]. The dependence of ICF fraction on various entrance channel parameters has also been studied. The present paper is organized as follows: A brief description of the experimental details is given in Sec. II and the Sec. III deals with the details of analysis of the data and its interpretation while a brief summary of the present work is given in Sec. IV of this paper.

II. EXPERIMENTAL DETAILS

The experiment for the system $^{14}\text{N} + ^{181}\text{Ta}$ was carried out at the ion-beam facility of the Inter University Accelerator Centre (IUAC), New Delhi, India. It may be pointed out here that negative ions of elements having negative electron affinity like ^{14}N cannot be produced in elemental form. The electron affinity of nitrogen is -0.07 eV. Such beams are produced in molecular form containing element required in the beam. As such, in case of ^{14}N , the CN molecules are injected into the accelerator. As this molecular beam passes through the stripper, the accelerated beam in molecular form gets dissociated and stripped forming positive ions of interest. These positive ions are accelerated downward through the accelerator column. The final selection of ^{14}N and its energy is carried out with help of magnetic analyzer for getting the required beam. In the present case $^{14}\text{N}^{6+}$ ions were finally taken in beam form for the experiment using 15UD Pelletron accelerator. In order to determine the reaction cross section, the activation/stacked foil technique followed by γ -ray spectroscopy was used. The α -transmission method was used to determine the thickness of each target. This method is based on the measurement of energy lost by α particles while passing through the target material. In this method, 5.486 MeV α particles obtained from ^{241}Am source were allowed to pass through the sample foil to estimate the energy loss of α particle in the sample thickness. The α -particle spectrometer was used for this purpose. Isotopically pure ^{181}Ta targets (purity 99.98%) and aluminum catcher/energy-degrader foils (thickness ≈ 1.2 –1.7 mg/cm 2) were prepared by using rolling technique. The Al-catcher foils were used for the dual purpose of degrading the incident beam energy and also to trap the reaction residues ejecting out from the target foil. The reaction products were trapped either in the target foil itself or in the Al-catcher foil put behind the target. All samples were cut into 1.2×1.2 cm 2 and pasted on Al holders having concentric hole of diameter 1.0 cm 2 . The Al holders are generally used for rapid dissipation of heat produced during irradiation. These holders were then screwed to the sample holding ladder of the scattering chamber where irradiation was carried out. While performing the experiments, three stacks each consisting of four target-catcher foil assemblies were irradiated separately at energies

87.07 \pm 0.93, 85.17 \pm 0.83, and 83.05 \pm 0.95 MeV so that energy interval between two successive samples will be minimum (less than 2 MeV). In the present work, the cross-section data of the reaction residues has been measured at 12 energy points between \approx 65 and 88 MeV. The irradiations were carried out in the General Purpose Scattering Chamber (GPSC) [32] having an in-vacuum transfer facility (ITF). Using the ITF, the samples can be taken out of the GPSC without disturbing its vacuum. Keeping in mind the half-lives of interest, the irradiation for each stack was carried out for \approx 8–10 h. The beam current was monitored during the irradiation by using a Faraday cup installed downstream the beam line connected to an ORTEC's current integrator and was maintained nearly constant \approx 25–30 nA. In order to check the accuracy of the beam flux obtained from the beam current, an auxiliary experiment was carried out in which two surface barrier detectors (Rutherford monitors) were kept at 30° with respect to the incident beam at forward angles to record the elastically scattered incident ions. The flux was calculated from the recorded count rates of Rutherford monitors using the well-known Rutherford formula. The magnitude of the flux of incident ion beam determined from the counts of Rutherford monitors and the integrated counts of the Faraday cup were found to agree with each other within 5%. The activity induced in each sample was recorded separately at increasing time intervals using an HPGe detector (100cc active volume) coupled to CAMAC-based data acquisition system CANDLE [33]. The resolution of HPGe spectrometer was 1.2 keV for the 1.33-MeV γ ray of ^{60}Co . Each sample-catcher foil assembly was counted separately. The energy and efficiency calibrations of the γ spectrometer were done prior to its use by employing the standard γ sources, viz., ^{22}Na , ^{60}Co , ^{133}Ba , and ^{152}Eu . The calibration was checked several times while carrying out the experiment. In the present, the standard γ sources used to determine efficiency and the irradiated target-catcher foil assemblies were counted in the same geometry with respect to the detector in order to avoid errors due to solid angle effects. Care was taken to keep the dead time of the detector \leq 10% by suitably adjusting the source-detector separation for each irradiated sample. However, the corrections for the dead time were made.

III. MEASUREMENTS AND INTERPRETATION OF RESULTS

To measure the EFs of residues populated through CF and/or ICF processes, the reaction residues were identified from the recorded γ -ray spectrum by their characteristic γ rays. The identification of populated residues was also done by the decay curve analysis. As a representative case, the relevant portion of the γ -ray spectrum of $^{14}\text{N} + ^{181}\text{Ta}$ recorded at energy 87.07 \pm 0.93 MeV is shown in Fig. 2. Further, the decay curves of the reaction residue ^{190}Hg formed via 5n channel identified with two different γ rays of 142.5 and 171.6 keV are shown in Fig. 3. As can be seen from Fig. 3 that the observed half-life of $^{190}\text{Hg}(5n)$ deduced from the decay curves was found to be consistent with each other and also in good agreement with the literature value. This confirms the production of the residues ^{190}Hg via 5n channel. A similar procedure

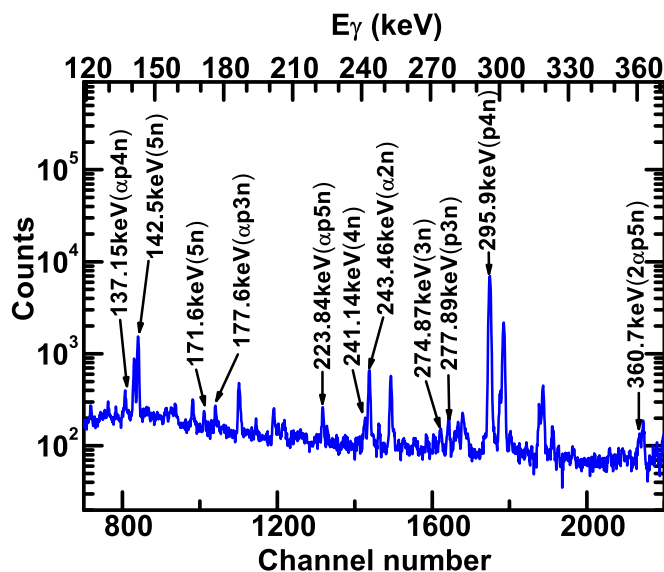


FIG. 2. A typical γ -ray spectrum of $^{14}\text{N} + ^{181}\text{Ta}$ at 87.07 \pm 0.93 MeV.

was adopted to confirm the identification of the other reaction residues. The spectroscopic data like half-lives, γ -ray energies and intensities, etc., of the identified reaction residues was taken from the Table of Isotopes [34] and Nuclear Wallet Card [35] and are listed in Table I. It may be noted that the residues populated in the interaction of ^{14}N with ^{181}Ta are expected to be formed by the deexcitation of CF and ICF composite systems [36].

The production cross sections for identified reaction residues populated via CF and/or ICF reactions were determined at each energy using the standard formulation [37]. However, uncertainties may arise in the measured cross section because of the experimental limitations [38]. The overall error, which includes the statistical error was estimated to be \leq 15%. The experimentally measured cross section for the

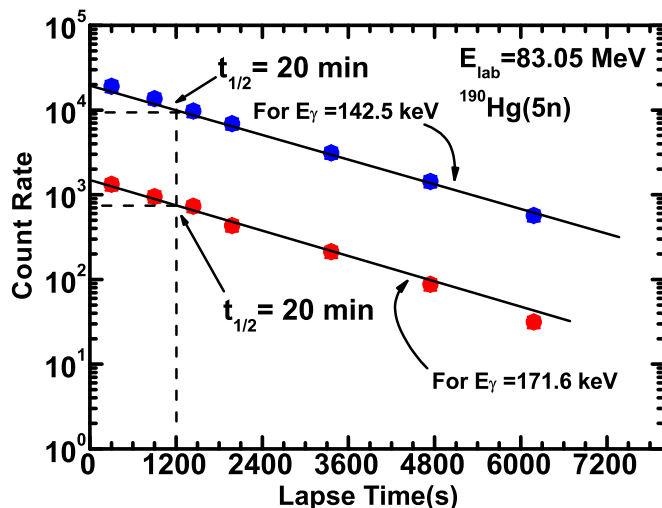


FIG. 3. Decay curve of the reaction residue $^{190}\text{Hg}(5n)$ for 142.5-keV and 171.6-keV γ -ray energy.

TABLE I. A list of identified reaction residues populated in $^{14}\text{N} + ^{181}\text{Ta}$ system and other properties.

Residue	Half-life	J^π	E_γ (keV)	I_γ (%)
$^{192}\text{Hg}(3n)$	4.85 h	0^+	274.87	50.4
$^{191}\text{Hg}^g(4n)$	49 min	$3/2^-$	241.14	8.86
$^{191}\text{Hg}^m(4n)$	50.8 min	$13/2^+$	241.14	12.4
$^{190}\text{Hg}(5n)$	20 min	0^+	142.5	54
			171.6	3.8
$^{189}\text{Hg}^g(6n)$	7.6 min	$3/2^-$	238.7	13.05
$^{189}\text{Hg}^m(6n)$	8.6 min	$13/2^+$	238.7	8.32
$^{191}\text{Au}^g(p3n)$	3.18 h	$3/2^+$	277.89	6.8
$^{190}\text{Au}^g(p4n)$	42.8 min	1^-	295.9	71
$^{189}\text{Au}^g(p5n)$	28.7 min	$1/2^+$	447.52	11
$^{189}\text{Au}^m(p5n)$	4.59 min	$11/2^-$	321.1	15.96
$^{189}\text{Pt}(\alpha 2n)$	10.87 h	$3/2^-$	243.46	4.1
$^{187}\text{Pt}(\alpha 4n)$	2.35 h	$3/2^-$	122.15	6.58
$^{186}\text{Pt}(\alpha 5n)$	2.0 h	0^+	689.2	84.24
$^{187}\text{Ir}^g(\alpha p3n)$	10.5 h	$3/2^+$	177.6	8.73
$^{186}\text{Ir}^g(\alpha p4n)$	15.8 h	5^+	137.15	41
$^{186}\text{Ir}^m(\alpha p4n)$	2.0 h	2^-	137.15	23
$^{185}\text{Ir}(\alpha p5n)$	14.4 h	$5/2^-$	223.84	7.48
$^{183}\text{Os}^g(2\alpha 4n)$	13.0 h	$9/2^+$	381.7	77
$^{181}\text{Re}(2\alpha p5n)$	19.9 h	$5/2^+$	360.7	20

residues populated via CF and/or ICF processes are tabulated in Tables II–IV.

The experimentally measured EFs were analyzed within the framework of statistical model code PACE4 [31], which is based on the Hauser-Feshbach theory of CN decay [39]. The details of the code are given in some of our earlier publications [11,12]. However, some of the important details are given here for the sake of completeness. In this code, the level density parameter a ($a = A/K \text{ MeV}^{-1}$) is one of the important parameters and the value of K can be varied in order to match the experimental data. Here A is the atomic mass number. In this code, an optical model subroutine calculate the transmission coefficient for neutron, proton, and α particles. The Bass model [21] is used to get the fusion cross section.

The partial fusion cross section σ_l is given by

$$\sigma_l = \pi \lambda^2 (2l + 1) T_l, \quad (1)$$

where λ is reduced wavelength and T_l is transmission coefficient given by

$$T_l = \frac{1}{1 + \exp\left(\frac{l - l_{\max}}{\Delta}\right)}, \quad (2)$$

where Δ is the diffuseness coefficient and l_{\max} is the maximum angular momentum, the value of which is obtained from the total fusion cross section σ_F ; $\sigma_F = \sum \sigma_l$.

It should be noted that PACE4 [31] is a complete fusion model code and it does not take into account any contribution coming from the break-up reactions. Therefore, any enhancement in the experimental cross-section values over the corresponding theoretical values may be attributed to the incomplete fusion reactions. The analysis of EFs for the identified reaction residues expected to be populated by CF and/or ICF reactions are discussed in the following subsections.

A. Excitation function of reaction residues populated via CF process

The measured EFs for several reaction residues populated via CF process are compared with the predictions of theoretical model code PACE4 [31]. In the present work, the EFs for the reactions $^{181}\text{Ta}(^{14}\text{N}, 3n)^{192}\text{Hg}$, $^{181}\text{Ta}(^{14}\text{N}, 4n)^{191}\text{Hg}^{g+m}$, $^{181}\text{Ta}(^{14}\text{N}, 5n)^{190}\text{Hg}$, and $^{181}\text{Ta}(^{14}\text{N}, 6n)^{189}\text{Hg}^{g+m}$, which are populated via CF process have been measured and are shown in Figs. 4(a)–4(d) respectively. Here, the reaction residues ^{191}Hg and ^{189}Hg have been populated by both ground and metastate, as indicated in Table I. The reaction $^{181}\text{Ta}(^{14}\text{N}, p5n)^{189}\text{Au}$ has both the metastable as well as ground states having 4.59- and 28.7-min half-lives, respectively, with independent γ rays. Thus, cross sections for both the states are measured separately and total cross section of $^{189}\text{Au}(p5n)$ is obtained by the sum of both the states. Further, in case of $^{190}\text{Au}(p4n)$ channel, the isomeric state of ^{190}Au decays with 125 ms half-life and the ground state of ^{190}Au has a half-life of 42.8 min and undergoes electron capture

TABLE II. Experimentally measured production cross sections for the residues populated in the $^{14}\text{N} + ^{181}\text{Ta}$ system via CF processes.

E_{lab} (MeV)	$^{192}\text{Hg}(3n)$ σ (mb)	$^{191}\text{Hg}^{g+m}(4n)$ σ (mb)	$^{190}\text{Hg}(5n)$ σ (mb)	$^{189}\text{Hg}^{g+m}(6n)$ σ (mb)
65.53 ± 1.09	1.6 ± 0.24	11.6 ± 1.74	–	–
67.50 ± 1.08	3.75 ± 0.56	65 ± 9.75	–	–
69.47 ± 1.06	5.8 ± 0.87	89.6 ± 13.44	–	–
71.54 ± 1.08	5.2 ± 0.78	192.4 ± 28.86	103 ± 15.35	–
73.65 ± 0.95	5.1 ± 0.76	154 ± 23.1	211 ± 31.65	–
75.65 ± 0.99	3.5 ± 0.52	119.6 ± 17.94	324 ± 48.6	–
77.08 ± 1.07	3.3 ± 0.49	125 ± 18.75	407 ± 61.05	–
79.51 ± 0.89	2.0 ± 0.30	72.3 ± 10.84	530 ± 79.5	–
81.42 ± 0.99	1.15 ± 0.17	38 ± 5.7	635 ± 95.25	–
83.05 ± 0.94	1.04 ± 0.15	35 ± 5.25	682 ± 102.3	19 ± 2.9
85.17 ± 0.83	0.68 ± 0.10	19 ± 2.85	714 ± 107.1	73 ± 10.95
87.07 ± 0.93	0.5 ± 0.07	10 ± 1.5	687 ± 103.05	148.5 ± 22.3

TABLE III. Experimentally measured production cross sections for the residues populated in the $^{14}\text{N} + ^{181}\text{Ta}$ system via CF processes.

E_{lab} (MeV)	$^{191}\text{Au}(p3n)$ σ^{cum} (mb)	$^{191}\text{Au}(p3n)$ σ^{ind} (mb)	$^{190}\text{Au}^g(p4n)$ σ^{cum} (mb)	$^{190}\text{Au}(p4n)$ σ^{ind} (mb)	$^{189}\text{Au}^{g+m}(p5n)$ σ^{cum} (mb)	$^{189}\text{Au}(p5n)$ σ^{ind} (mb)
65.53 ± 1.09	16 ± 2.4	0.2 ± 0.03	–	–	–	–
67.50 ± 1.08	89 ± 13.34	0.9 ± 0.14	12 ± 1.8	–	–	–
69.47 ± 1.06	124.6 ± 18.7	3.2 ± 0.15	37.1 ± 5.57	–	–	–
71.54 ± 1.08	268.8 ± 40.32	8 ± 1.2	193.43 ± 29.01	0.10 ± 0.02	–	–
73.65 ± 0.95	222 ± 33.3	13 ± 1.95	396.8 ± 59.52	0.75 ± 0.11	–	–
75.65 ± 0.99	178.1 ± 26.7	16 ± 2.4	611 ± 91.65	2.85 ± 0.43	–	–
77.08 ± 1.07	184.4 ± 27.6	15 ± 2.25	769 ± 115.35	5.06 ± 0.76	–	–
79.51 ± 0.89	109 ± 16.35	11 ± 1.65	1003 ± 150.45	8.19 ± 1.23	–	–
81.42 ± 0.99	59.5 ± 8.9	8 ± 1.2	1205 ± 180.75	13.1 ± 1.96	–	–
83.05 ± 0.94	53.5 ± 8.02	6 ± 0.9	1299 ± 194.85	18.9 ± 2.83	26.7 ± 4.0	0.46 ± 0.07
85.17 ± 0.83	30 ± 4.5	4.25 ± 0.64	1362 ± 204.3	21.8 ± 3.27	103 ± 15.45	2.19 ± 0.33
87.07 ± 0.93	16 ± 2.4	2.45 ± 0.37	1314 ± 197.1	24.5 ± 3.67	211 ± 31.65	5.94 ± 0.89

(EC) decay independently. In case of ^{191}Au residues populated via $p3n$ channel, both ground as well as metastable states are populated. The metastable state which has a lifetime of 0.92-s decays directly to ground state of ^{191}Au . As such, the total cross section of $^{191}\text{Au}(p3n)$ is measured. During the decay curve analysis, the cross sections for reaction residues $^{191}\text{Au}^g(p3n)$ ($t_{1/2} = 3.18$ h), $^{190}\text{Au}^g(p4n)$ ($t_{1/2} = 42.8$ min), and $^{189}\text{Au}^{g+m}(p5n)$ ($t_{1/2}^g = 28.7$ min, $t_{1/2}^m = 4.59$ min) were found to be strongly fed from their higher charge isobar precursor $^{191}\text{Hg}(4n)$, $^{190}\text{Hg}(5n)$, and $^{189}\text{Hg}(6n)$, respectively, through β^+ /EC decay. The cumulative cross sections ($\sigma_{\text{cum}} = \sigma_{\text{ind}} + \sigma_{\text{pre}}$) for the residues $^{191}\text{Au}(p3n)$, $^{190}\text{Au}(p4n)$, and $^{189}\text{Au}(p5n)$ are shown in Figs. 5(a)–5(c) respectively. In order to determine the independent cross section (σ_{ind}) for ^{191}Au , ^{190}Au , and ^{189}Au residues, the successive radioactive decay formulations proposed by Cavinato *et al.* [40], based on the Bateman equations [41] were used as

$$\sigma_{\text{ind}} = \sigma_{\text{cum}} - P_{\text{pre}} \frac{t_{1/2}^d}{(t_{1/2}^d - t_{1/2}^{\text{pre}})} \sigma_{\text{pre}}. \quad (3)$$

In the above equation, $t_{1/2}^d$ and $t_{1/2}^{\text{pre}}$ represent the half-lives of daughter and precursor nuclei, respectively. The P_{pre} is the branching ratio from precursor to its daughter nuclei. The values of half-lives and branching ratio of the precursor decay (P_{pre}) were taken from Refs. [34,35]. The deduced independent cross section (σ_{ind}) for the reaction residues ^{191}Au , ^{190}Au , and ^{189}Au are shown in Figs. 5(d)–5(f), respectively.

The effect of variation of parameter K ($K = 8$ – 10) of the code PACE4 on calculated values of cross section for the residues ^{192}Hg , ^{191}Hg , ^{190}Hg , and ^{189}Hg are also shown in Figs. 4(a)–4(d), respectively. In these figures, the experimental values of cross sections are shown. As can be seen from these figures, the experimental EFs of xn channels are well matched with PACE4 predictions for the level density parameter $a = A/10$ MeV $^{-1}$, indicating their production solely via CF process. However, slowly decreasing tail of the excitation function for the $3n$ channel [Fig. 4(a)] has been observed which is the characteristic of precompound emission. Further, the same value of the level density parameter $a = A/10$ MeV $^{-1}$ is found to reproduce pxn channels satisfactorily and are shown in Figs. 5(d)–5(f), which confirms their production only through CF. Hence, in the present work, the value of

TABLE IV. Experimentally measured production cross sections for the residues populated in the $^{14}\text{N} + ^{181}\text{Ta}$ system via CF and/or ICF processes.

E_{lab} (MeV)	$^{189}\text{Pt}(\alpha 2n)$ σ (mb)	$^{187}\text{Pt}(\alpha 4n)$ σ (mb)	$^{186}\text{Pt}(\alpha 5n)$ σ (mb)	$^{187}\text{Ir}(\alpha p 3n)$ σ (mb)	$^{186}\text{Ir}^{g+m}(\alpha p 4n)$ σ (mb)	$^{185}\text{Ir}(\alpha p 5n)$ σ (mb)	$^{183}\text{Os}^g(2\alpha 4n)$ σ (mb)	$^{181}\text{Re}(2\alpha p 5n)$ σ (mb)
67.50 ± 1.08	0.6 ± 0.09	–	–	–	–	–	–	–
69.47 ± 1.06	1.0 ± 0.15	1.3 ± 0.2	–	–	–	–	–	0.4 ± 0.06
71.54 ± 1.08	1.6 ± 0.24	4.8 ± 0.7	–	–	–	–	–	0.6 ± 0.1
73.65 ± 0.95	1.4 ± 0.21	9 ± 1.35	–	–	–	–	–	1 ± 0.15
75.65 ± 0.99	1.0 ± 0.15	14 ± 2.1	–	–	–	0.08 ± 0.01	–	1.3 ± 0.2
77.08 ± 1.07	0.7 ± 0.11	19.2 ± 2.9	–	0.14 ± 0.02	–	0.2 ± 0.03	0.24 ± 0.04	1.4 ± 0.22
79.51 ± 0.89	0.4 ± 0.06	24 ± 3.6	–	0.2 ± 0.03	0.3 ± 0.05	0.4 ± 0.06	0.46 ± 0.07	2 ± 0.3
81.42 ± 0.99	0.5 ± 0.08	32 ± 4.8	1 ± 0.15	0.42 ± 0.06	0.5 ± 0.08	0.8 ± 0.12	0.56 ± 0.08	2.45 ± 0.37
83.05 ± 0.94	0.5 ± 0.08	35 ± 5.3	2 ± 0.3	0.48 ± 0.07	0.8 ± 0.12	1.0 ± 0.15	0.72 ± 0.1	2.9 ± 0.43
85.17 ± 0.83	0.8 ± 0.12	38 ± 5.7	5 ± 0.75	1 ± 0.15	2 ± 0.3	1.8 ± 0.27	1 ± 0.15	3 ± 0.45
87.07 ± 0.93	1.3 ± 0.20	40 ± 6	7 ± 1.05	1.4 ± 0.21	3 ± 0.5	3.0 ± 0.45	1.26 ± 0.2	3.5 ± 0.53

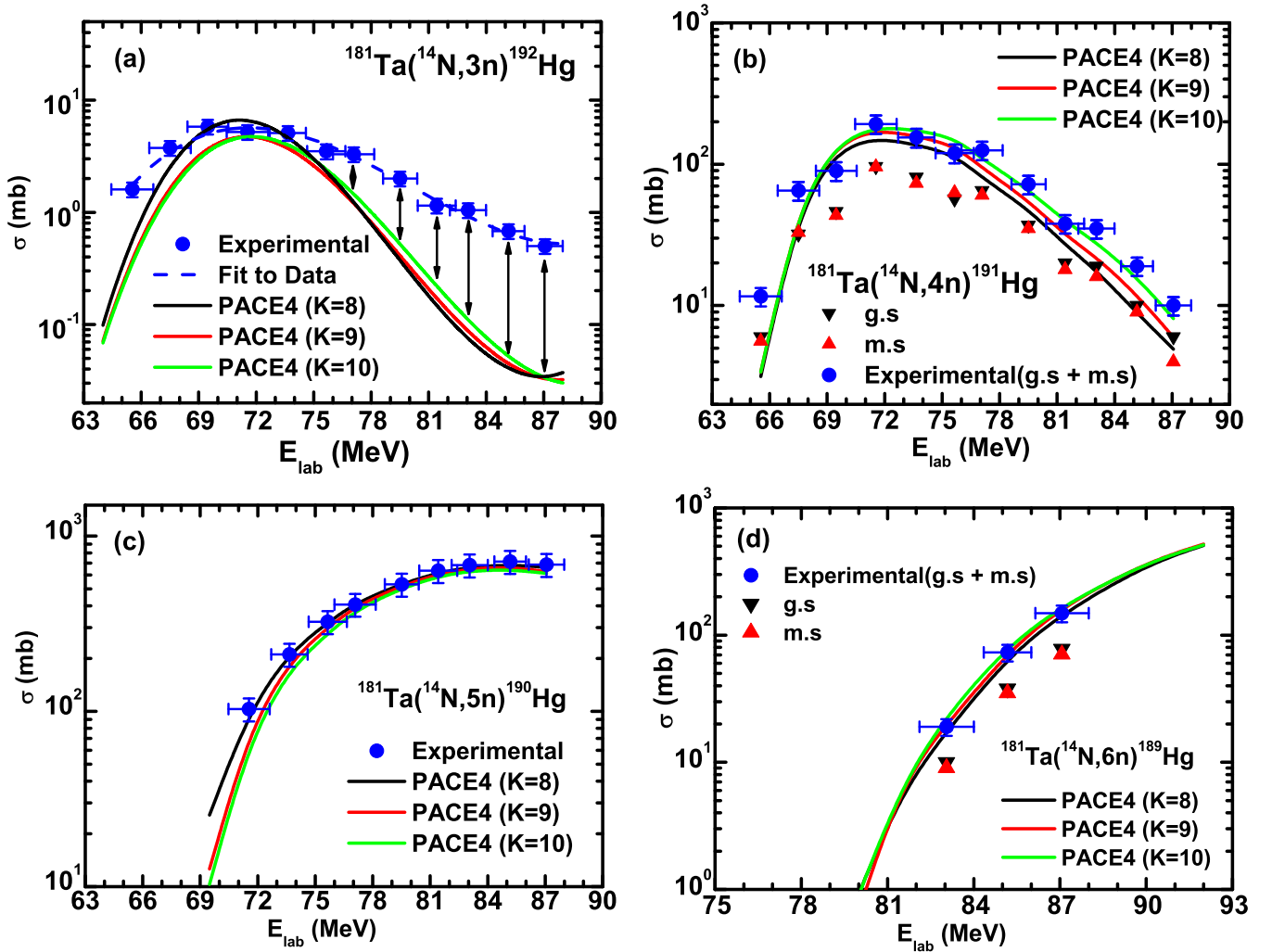


FIG. 4. Experimentally measured and theoretically calculated EFs of residues (a) ^{192}Hg populated via $3n$ channel, (b) $^{191}\text{Hg}^{g+m}$ populated via $4n$ channel, (c) ^{190}Hg populated via $5n$ channel, and (d) $^{189}\text{Hg}^{g+m}$ populated via $6n$ channel, in the interaction of $^{14}\text{N} + ^{181}\text{Ta}$ system

level density parameter a is kept fixed ($a = A/10 \text{ MeV}^{-1}$) for the analysis of other reaction channels. It may also be noted that the statistical model code PACE4 uses the optical model potentials for neutron, proton, α particle, and other incoming channels. The optical model potential provides basis for many theoretical analysis and/or evaluations of nuclear cross sections. It consists of real and imaginary nuclear potential well. The default values for real part of nuclear potential well in code PACE4 were taken as 47.01, 63.66, and 50 MeV for neutron, proton, and α particle, respectively. It may be noted that for these values of default parameters, the experimental data for xn and pxn channels are found to be reproduced satisfactorily.

1. Observation of preequilibrium emission

It has now become well established [42,61] that in light ion induced reactions at moderate excitation energies, the compound and precompound emission compete with each other. It is well known that compound nucleus reactions were first verified by Ghoshal's experiment [62]. Recently,

both the intuition and results of experiments proved that the precompound emission becomes dominant as the energy of the incident particle increases. Some of the important signatures of precompound emission are (i) the slowly descending tails in the measured excitation functions, (ii) observation of high-energy particles as compared to the statistical model predictions, (iii) forward peaked angular distribution of emitted particles, etc. Some recent reports [63,64] indicate that the phenomenon of precompound emission has been observed in heavy-ion interactions as well. In the present work also, as can be seen that in case of measurement of excitation function for $^{181}\text{Ta}(^{14}\text{N}, 3n)^{192}\text{Hg}$ reaction [Fig. 4(a)], the high-energy tail portion has been observed as compared to statistical model predictions of code PACE4. The difference between the experimental cross section and the PACE4 prediction may be attributed to the precompound emission. In order to see the dependence of precompound emission on energy in this reaction, the precompound fraction has been deduced. The precompound fraction f_{PE} may be defined as to give the relative strength of precompound emission with respect to the compound nucleus emission. The f_{PE} has been derived

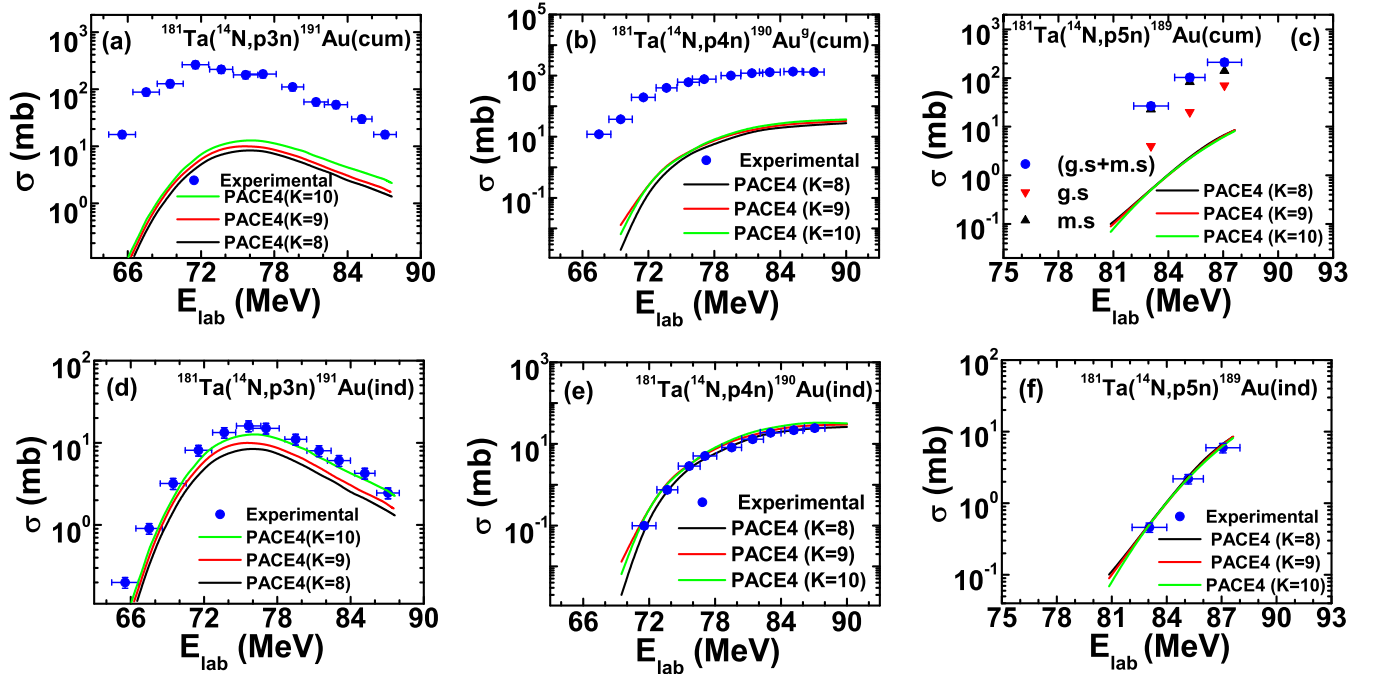


FIG. 5. Experimentally measured and theoretically calculated EFs of residues $^{191}\text{Au}(p3n)$, $^{190}\text{Au}(p4n)$, and $^{189}\text{Au}(p5n)$: (a) cumulative and (d) independent cross section of ^{191}Au residue; (b) cumulative and (e) independent cross section of ^{190}Au residue; and (c) cumulative and (f) independent cross section of ^{189}Au residue populated in $^{14}\text{N} + ^{181}\text{Ta}$ system.

as $\{[\sigma_{\text{exp}(3n)} - \sigma_{\text{PACE}(3n)}] / \sigma_{\text{exp}(3n)}\}$. The deduced f_{PE} has been plotted as a function of beam energy in Fig. 6. As can be seen, the f_{PE} increases with energy for this channel and approaches to nearly 100% at relatively higher energies. Thus, there is strong dependence of preequilibrium emission with energy for 3n channel. Hence, it may be confirmed that even in heavy-ion collisions the precompound emission also competes with complete fusion for some neutron emitting channels.

B. Excitation function of reaction residues populated via CF and/or ICF process

The experimentally measured excitation functions of residues populated in α -emitting reaction channels,

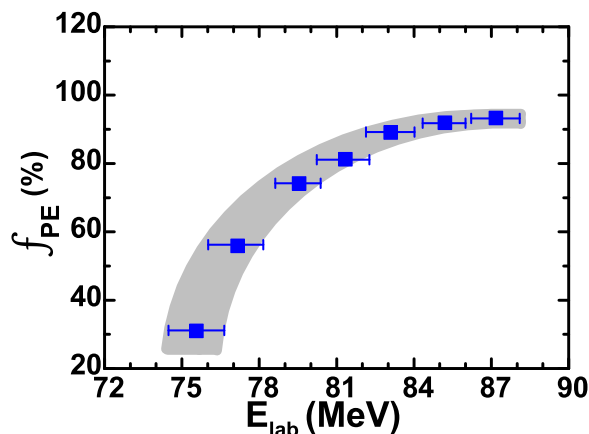


FIG. 6. Variation of precompound fraction (f_{PE}) with beam energy.

i.e., $^{189}\text{Pt}(\alpha 2n)$, $^{187}\text{Pt}(\alpha 4n)$, $^{186}\text{Pt}(\alpha 5n)$, $^{187}\text{Ir}^g(\alpha p3n)$, $^{186}\text{Ir}^{g+m}(\alpha p4n)$, $^{185}\text{Ir}(\alpha p5n)$, $^{183}\text{Os}^g(2\alpha 4n)$, and $^{181}\text{Re}(2\alpha p5n)$ expected to be populated by the complete fusion and incomplete fusion processes are shown in Figs. 7 and 8. It may be remarked that the residues $^{187}\text{Ir}(\alpha p3n)$ are populated both in ground and metastable states. The metastable state has a half-life of 30.3 ms and decays to ground state, as such total cross section of $^{187}\text{Ir}(\alpha p3n)$ has been measured. Further, the residues $^{183}\text{Os}(2\alpha 4n)$ are populated both in metastable and ground state but the intensities of γ rays of the metastable state are very low and hence could not be observed. The analysis of these reaction residues has been performed by keeping the same values of parameters of code PACE4, as were used for CF channels discussed in the previous section. The effect of different values of free parameter $K(=8-10)$ on theoretical calculations is also shown in Figs. 7(a)–7(d). It may be noted from these figures that the experimentally measured EFs of α channels show a significant enhancement over the PACE4 calculations. As already mentioned, the code PACE4 does not take into consideration the contribution from ICF reactions, as such the experimentally observed enhancement for α -emitting channels may be attributed to ICF processes. Further, there is a likelihood of precursor contribution in some of the residues studied presently which are populated via α -emitting channels as well. The residues $^{189}\text{Pt}(\alpha 2n)$, $^{187}\text{Ir}(\alpha p3n)$, and $^{186}\text{Ir}(\alpha p4n)$ may also have contribution from their higher charge isobar precursors $^{189}\text{Au}(p5n)$, $^{187}\text{Pt}(\alpha 4n)$, and $^{186}\text{Pt}(\alpha 5n)$, respectively, through β^+ /EC decay. As such, attempts were made to analyze the data within the framework of prescription given by Cavinato *et al.* [40] and it was found

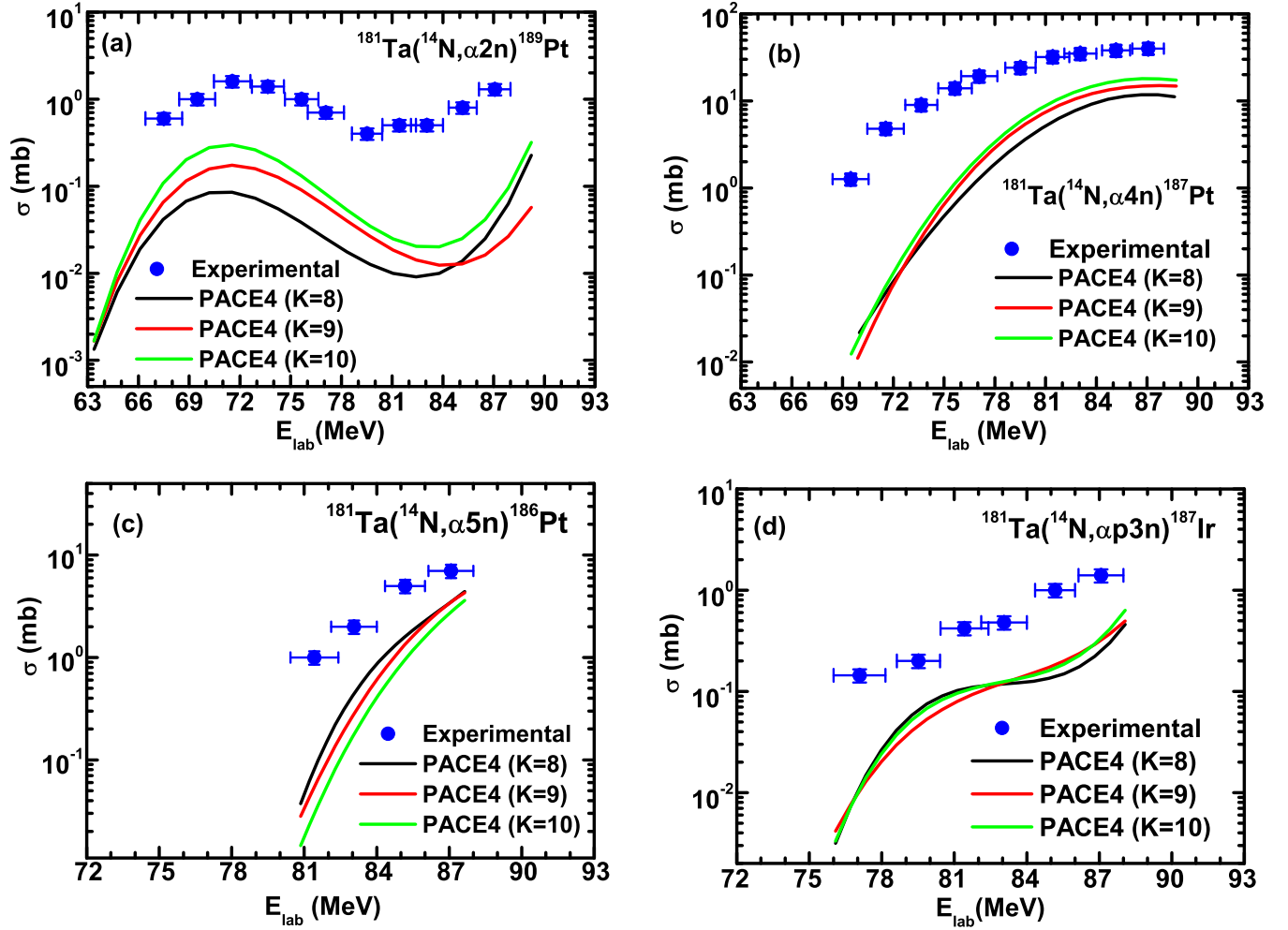
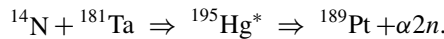


FIG. 7. Experimentally measured EFs of residues (a) ^{189}Pt populated via $\alpha 2n$ channel, (b) ^{187}Pt populated via $\alpha 4n$ channel, (c) ^{186}Pt populated via $\alpha 5n$ channel, and (d) ^{187}Ir populated via $\alpha p 3n$ channel, and their comparison with PACE4 predictions in the interaction of $^{14}\text{N} + ^{181}\text{Ta}$ system.

that the precursor contribution to these residues are almost negligible and hence not shown in the figures. It may again be remarked that there is no theoretical model to explain the α -emitting channels. Moreover, the Figs. 8(a)–8(d) show the experimental EFs of $^{186}\text{Ir}^{g+m}(\alpha p 4n)$, $^{185}\text{Ir}(\alpha p 5n)$, $^{183}\text{Os}^g(2\alpha 4n)$, and $^{181}\text{Re}(2\alpha p 5n)$ residues, respectively, for which the code PACE4 is found to give negligible values of cross section indicating that these residues are dominantly populated via ICF processes only. As mentioned above, the residues involving α particle(s) in the exit channel may be populated via both CF and/or ICF processes. For example, the residues ^{189}Pt can be populated in the following ways:

- (i) via the CF of ^{14}N with ^{181}Ta :

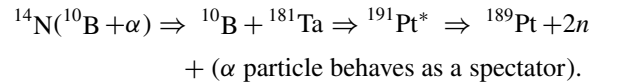


Here an α particle and two neutrons are emitted from the excited CN $^{195}\text{Hg}^*$.

- (ii) via incomplete fusion of ^{14}N with ^{181}Ta .

Here the projectile ^{14}N when comes near the field of target nucleus may break-up into fragments ($^{10}\text{B} + \alpha$)

and only one fragment (i.e., ^{10}B) fuses with ^{181}Ta to form an incompletely fused composite (IFC) system ($^{191}\text{Pt}^*$),



Here two neutrons are emitted from IFC system.

In the present work, the contribution of ICF processes for all the α -emitting channels was deduced by subtracting the PACE4 contributions for all α -evaporating channels from the total experimentally measured EFs for α channels. As such, the ICF cross section was deduced at each projectile energy as, $\sum \sigma_{\text{ICF}} = \sum \sigma_{\alpha xn + \alpha pxn + 2\alpha xn + 2\alpha pxn}^{\text{exp}} - \sum \sigma_{\alpha xn + \alpha pxn + 2\alpha xn + 2\alpha pxn}^{\text{PACE4}}$. The ICF cross section obtained as above has been used to get its dependence on various entrance channel parameters.

Any statistical model cannot perfectly reproduce the process of de-excitation. However, it is worthwhile to mention

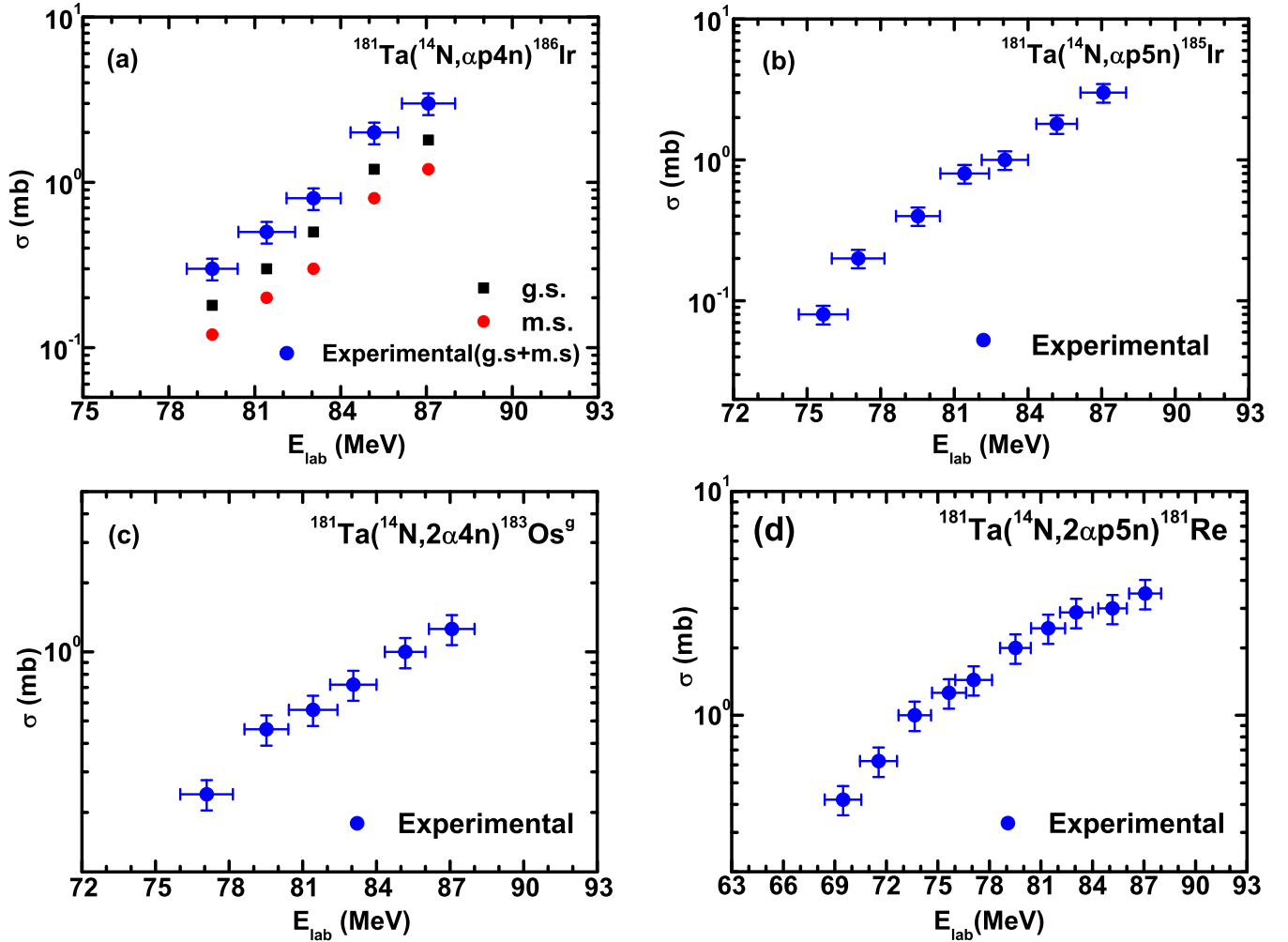


FIG. 8. Experimentally measured EFs of residues (a) $^{186}\text{Ir}^{g+m}$ populated via $\alpha p4n$ channel, (b) ^{185}Ir populated via $\alpha p5n$ channel, (c) $^{183}\text{Os}^g$ populated via $2\alpha 4n$ channel, and (d) ^{181}Re populated via $2\alpha p5n$ channel, in the interaction of $^{14}\text{N} + ^{181}\text{Ta}$ system. The theoretically calculated values are not shown in these figures as PACE4 predicts negligible cross sections for these channels.

that the measured excitation functions of individual reaction channels, in a given system, may be reproduced separately with different choice of parameters of the code indicating model dependency, but from the physics point of view this is not reasonable. Therefore, in the present work, calculations were performed for all the CF channels consistently with the same set of parameters as shown in Figs. 4(b)–4(d) and 5(d)–5(f). The same parameters which were used to fit CF channels have consistently been used to analyze the α -emitting channels as well. It may be observed from Figs. 7(a)–7(d) and 8(a)–8(d) that all the measured α -emitting channels are under predicted by PACE4 calculations, done consistently with the same set of parameters which satisfactorily explained the CF channels. As such, the experimentally observed higher production cross sections with respect to the theoretical predictions of the code may be attributed due to the incomplete fusion processes. In some of our publications [27,65,66], the direct and model independent methods like recoil range and angular distribution measurements, used to obtain the ICF contributions were found to reproduce the results deduced from the analysis of excitation function data using a consistent

set of parameters of the PACE4 model. Thus, a good agreement between the results of distinctly different methods of measurements give credence to the choice of parameters used in PACE4 calculations.

It may be remarked that the excitation functions of evaporation residues formed by CF process are well reproduced by PACE4 calculations which justify our measurements both quantitatively and qualitatively. Attempt has also been made to give strength to these measurements by deducing the value of Coulomb barrier (V_b) for the presently studied system ($^{14}\text{N} + ^{181}\text{Ta}$) with the help of experimentally measured fusion (evaporation) cross section ($\sigma_{\text{CF}}^{\text{exp}}$). The expression used for deducing the value of V_b is given below as [67]

$$\sigma_{\text{CF}} = \pi R^2 (1 - V_b/E_{\text{c.m.}}), \quad (4)$$

where V_b and $E_{\text{c.m.}}$ are the Coulomb barrier and incident energy in center-of-mass frame respectively and R is the interaction radius.

The measured data for complete fusion cross section ($\sigma_{\text{CF}}^{\text{exp}}$) is plotted as a function of $1/E_{\text{c.m.}}$ and is shown in Fig. 9. As expected, the fitting to data is a straight line which cuts

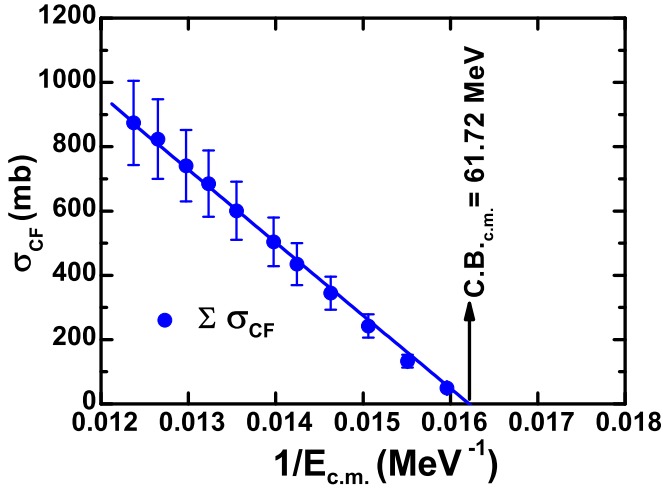


FIG. 9. A plot of complete fusion cross section with inverse of center-of-mass beam energy.

the x axis at the inverse of beam energy (equal to Coulomb barrier) in the center-of-mass frame and is found to be 61.72 MeV. The value of Coulomb barrier is found to agree well with that calculated theoretically which strengthens the accuracy of present measurements.

C. ICF strength function (F_{ICF}) and its variation with entrance channel parameters

In order to have a better insight on the onset of ICF and how the structure of projectile affects the ICF dynamics, the incomplete fusion strength function (F_{ICF}) is deduced and its dependence on various entrance channel parameters has been studied. The F_{ICF} is a measure of strength of ICF relative to the total fusion, is expressed as, $F_{ICF} = \sigma_{ICF}^{exp}/\sigma_{TF}$. Here σ_{ICF}^{exp} is the deduced experimental value of ICF cross section and σ_{TF} is the total fusion cross section. On the basis of dependence of (F_{ICF}) on various entrance channel parameters, one may be able to explain the reaction dynamics involved in the ICF processes.

1. Effect of projectile energy on ICF

To study the dependence of ICF on projectile energy, the F_{ICF} is plotted as a function of normalized beam energy and is shown in Fig. 10. It has been observed that the ICF fraction is found to be $\approx 0.4\%$ of σ_{TF} at $1.0145 V_b$ (i.e., 1.45% above the barrier). This may be considered to be the onset energy value of ICF for the presently studied system. The ICF fraction for the present system increases up to $\approx 6\%$ of σ_{TF} at the highest measured energy (87.07 ± 0.93 MeV) which is $\approx 30\%$ above the Coulomb barrier. This clearly suggests that ICF increases as the beam energy is increased. This can be explained on the basis of angular momentum because, as the beam energy increases, a larger input angular momenta is imparted to the system. As a result, the fusion pocket in the effective potential starts disappearing. In order to restore the fusion pocket and to provide sustainable angular momenta to the system for fusion, the projectile breaks-up into fragment(s) leading to the ICF process. The probability for fusion of one fragment or a group

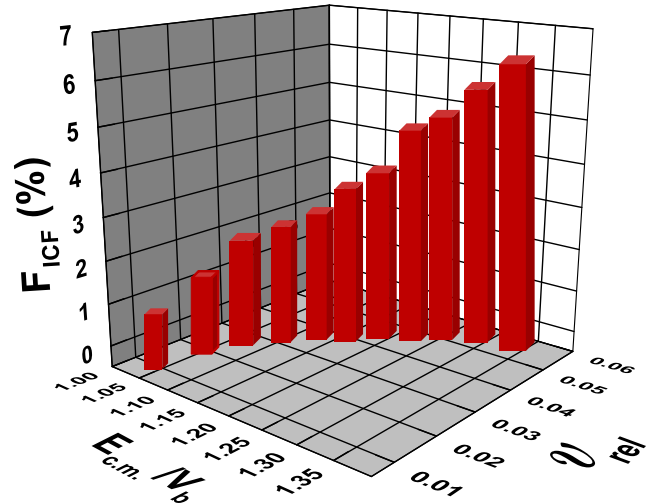


FIG. 10. A comparison of F_{ICF} values as a function of normalized beam energy and relative velocity (v_{rel}/c) for $^{14}\text{N} + ^{181}\text{Ta}$ system.

of fragments would depend entirely upon the value of input angular momenta. Figure 10 also shows the variation of F_{ICF} values with respect to the relative velocity of the colliding nuclei. As can be seen from this figure, F_{ICF} also increases with v_{rel} . The relative velocity of the colliding nuclei was calculated using the expression [68],

$$v_{rel} = [2(E_{c.m.} - V_b)/\mu]^{1/2}, \quad (5)$$

where μ is the reduced mass of the system and V_b is the Coulomb barrier in center-of-mass frame.

To see the influence of ICF on total fusion cross section $\sum \sigma_{TF}$ ($= \sum \sigma_{CF}^{exp} + \sum \sigma_{ICF}^{exp}$), the values of $\sum \sigma_{TF}$, $\sum \sigma_{CF}^{exp}$, and $\sum \sigma_{ICF}^{exp}$ are deduced with respect to projectile energy and are shown in Table V. It may be remarked that the $\sum \sigma_{ICF}^{exp}$ shown in Fig. 11, is the lower limit of ICF contribution because some of the channels could not be identified due to experimental limitations. However, the variation of $\sum \sigma_{ICF}^{exp}$ as a function of projectile energy is shown in the Fig. 11. The onset of ICF at energies just above the Coulomb barrier has

TABLE V. Values of total fusion, total complete fusion, and total incomplete fusion cross section at each incident energy is shown in this table.

Energy (MeV)	$\sum \sigma_{TF}$ (mb)	$\sum \sigma_{CF}^{exp}$ (mb)	$\sum \sigma_{ICF}^{exp}$ (mb)
65.53 ± 1.09	13.4 ± 2.01	13.4 ± 2.01	–
67.50 ± 1.08	49.96 ± 7.53	49.36 ± 7.40	0.2 ± 0.03
69.47 ± 1.06	135.53 ± 15.23	132.85 ± 14.68	1.68 ± 0.26
71.54 ± 1.08	249.26 ± 37.5	242.25 ± 36.15	5.04 ± 0.78
73.65 ± 0.95	355.96 ± 50.7	344.44 ± 48.51	8.28 ± 1.29
75.65 ± 0.99	450.47 ± 72.22	434.56 ± 69.08	11.77 ± 1.84
77.08 ± 1.07	525.83 ± 83.07	503.92 ± 79.03	16.94 ± 2.64
79.51 ± 0.89	628.72 ± 99.55	600.78 ± 94.61	22.58 ± 3.54
81.42 ± 0.99	723.49 ± 105.52	685.16 ± 99.02	33.13 ± 5.13
83.05 ± 0.94	785 ± 110.54	740.78 ± 103.31	38.56 ± 6.01
85.17 ± 0.83	876.15 ± 120.17	823.68 ± 111.7	48.73 ± 7.61
87.07 ± 0.93	934.40 ± 133.48	874.12 ± 124.1	57.64 ± 9.10

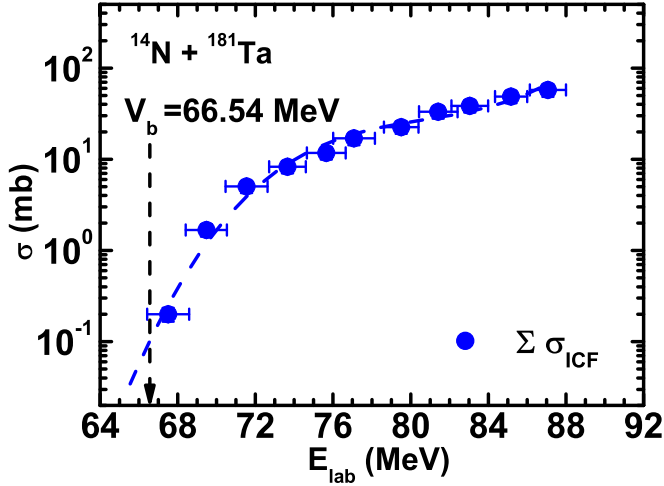


FIG. 11. A Variation of $\sum \sigma_{ICF}$ as a function of projectile energy. Lines through the data points are drawn to guide the eyes. The vertical error bars are embedded into data points.

been observed. Thus, ICF starts competing even at energies close to the barrier. It is clear from this figure that the ICF cross section is found to increase with beam energy, indicating its importance at relatively higher energies. The incomplete fusion strength function (F_{ICF}) has been deduced from the experimentally measured EFs and compared with the F_{ICF} values of other projectiles (both α -cluster and non- α -cluster) on different targets and discussed in the following sections. The value of l_{crit} for the presently studied system is $66\hbar$, however, the value of l_{max} at lowest energy (67.5 ± 1.08 MeV) where ICF has been observed is $9\hbar$. As such, it may also be concluded that ICF starts contributing even below l_{crit} .

2. Effect of Coulomb factor ($Z_p Z_T$) on ICF

The dependence of ICF has also been evaluated in terms of product of charges of the projectile and target nuclei ($Z_p Z_T e^2$), where Z_p and Z_T are the atomic numbers of projectile and target nuclei, respectively, and e is the electronic charge. The strength of ICF as a function of $Z_p Z_T$ for the presently studied system and those taken from literature have been deduced and are shown in Fig. 12. The available systems studied along with their $Z_p Z_T$ and α - Q values are given in Table VI. As can be seen from the Fig. 12, the ICF fraction follows a linearly increasing trend with $Z_p Z_T$. It is due to the fact that as the projectile approaches the target nucleus, the Coulomb repulsion acting between them is increased and hence due to this strong repulsion, the projectile detaches α particle(s) which acts as a spectator and the remaining part of the projectile fuses with the target nucleus leading to ICF process. Thus, an increase in the value of $Z_p Z_T$ enhances the probability of breaking of the projectile nucleus resulting in the increase in the probability of ICF processes. Figure 12 also gives a self explanation for breakup of α -cluster and non- α -cluster projectiles. As can be seen from this figure that F_{ICF} lies on the same straight line (black dotted line) for all α -cluster projectiles (^{12}C and ^{16}O). However, for non- α -cluster projectiles (^{19}F , ^{13}C and ^{14}N),

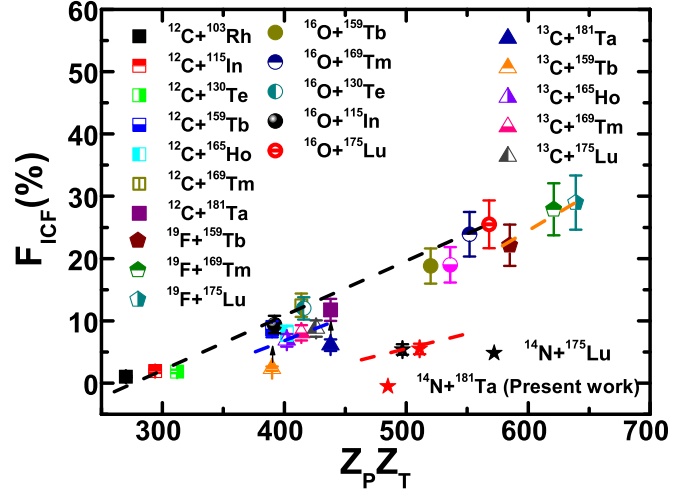


FIG. 12. A comparison of percentage of incomplete fusion fraction values for different systems as a function of $Z_p Z_T$ at constant relative velocity ($v_{rel} = 0.053c$). The colored dashed lines are drawn to guide the eyes (for further details, see text).

separate straight lines with successively decreasing values of F_{ICF} are obtained.

It may be inferred from the obtained trends of F_{ICF} with $Z_p Z_T$ for different projectiles (both α -cluster and non- α -cluster) that structural effects of the projectile plays a

TABLE VI. List of systems along with their entrance channel parameters: $Z_p Z_T$ is the product of atomic numbers of interacting partners and Q_α is the α - Q value of the projectile.

System	$Z_p Z_T$	Q_α (MeV)	Ref.
$^{12}\text{C} + ^{103}\text{Rh}$	270	-7.367	[43]
$^9\text{Be} + ^{181}\text{Ta}$	292	-2.648	[59]
$^{12}\text{C} + ^{115}\text{In}$	294	-7.367	[44]
$^{12}\text{C} + ^{130}\text{Te}$	312	-7.367	[45]
$^{12}\text{C} + ^{159}\text{Tb}$	390	-7.367	[46]
$^{13}\text{C} + ^{159}\text{Tb}$	390	-10.648	[11]
$^{16}\text{O} + ^{115}\text{In}$	392	-7.161	[47]
$^{12}\text{C} + ^{165}\text{Ho}$	402	-7.367	[48]
$^{13}\text{C} + ^{165}\text{Ho}$	402	-10.648	[49]
$^{12}\text{C} + ^{169}\text{Tm}$	414	-7.367	[50]
$^{13}\text{C} + ^{169}\text{Tm}$	414	-10.648	[51]
$^{16}\text{O} + ^{130}\text{Te}$	416	-7.161	[52]
$^{13}\text{C} + ^{175}\text{Lu}$	426	-10.648	[53]
$^{12}\text{C} + ^{181}\text{Ta}$	438	-7.367	[54]
$^{13}\text{C} + ^{181}\text{Ta}$	438	-10.648	[54]
$^{14}\text{N} + ^{175}\text{Lu}$	497	-11.62	[60]
$^{14}\text{N} + ^{181}\text{Ta}$	511	-11.62	Present work
$^{16}\text{O} + ^{159}\text{Tb}$	520	-7.161	[56]
$^{16}\text{O} + ^{165}\text{Ho}$	536	-7.161	[55]
$^{16}\text{O} + ^{169}\text{Tm}$	552	-7.161	[56]
$^{16}\text{O} + ^{175}\text{Lu}$	568	-7.161	[57]
$^{16}\text{O} + ^{181}\text{Ta}$	584	-7.161	[58]
$^{19}\text{F} + ^{159}\text{Tb}$	585	-4.014	[30]
$^{19}\text{F} + ^{169}\text{Tm}$	621	-4.014	[12]
$^{19}\text{F} + ^{175}\text{Lu}$	639	-4.014	[30]

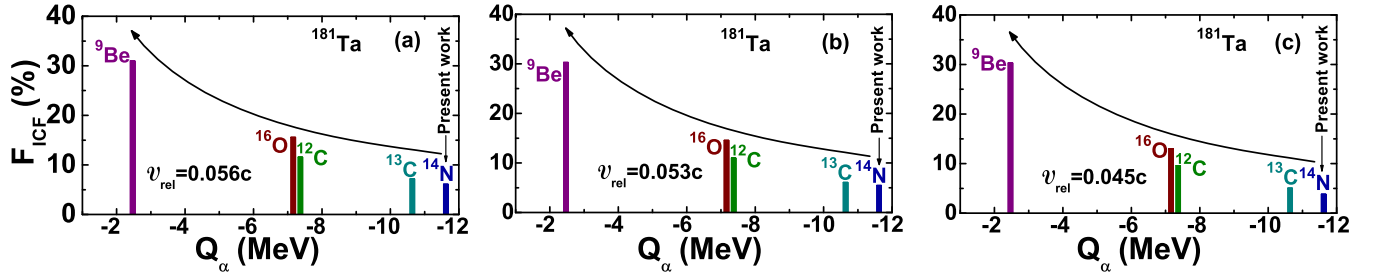


FIG. 13. A comparison of F_{ICF} in terms of Q_α value of the projectiles on same target ^{181}Ta at (a) $v_{\text{rel}} = 0.056c$, (b) $v_{\text{rel}} = 0.053c$, and (c) $v_{\text{rel}} = 0.045c$.

significant role in the ICF reaction dynamics. In order to verify the structural effects, the influence of α - Q values of different projectiles on F_{ICF} has been studied and is discussed in the next section.

3. Effect of projectile's Q_α value on ICF

The α - Q value of a projectile is defined as the energy required to separate out an α particle from the projectile nucleus. In order to understand the importance of structure effect of projectiles on ICF dynamics, the deduced values of F_{ICF} for the present system along with four other systems $^9\text{Be} + ^{181}\text{Ta}$ [59], $^{12,13}\text{C} + ^{181}\text{Ta}$ [54], and $^{16}\text{O} + ^{181}\text{Ta}$ [58] have been plotted in terms of α - Q value of the projectile and is shown in Figs. 13(a)–13(c) for three different values of v_{rel} ($v_{\text{rel}} = 0.056c, 0.053c, 0.045c$). It may be remarked that Morgenstern *et al.* [68] in their pioneer work showed that ICF fraction increases at $v_{\text{rel}} \geq 0.06c$. However, the present analysis indicates that there is a significant contribution from ICF processes even below $v_{\text{rel}} = 0.06c$. It may also be noted that ICF fraction for all systems decreases as the value of v_{rel} is decreased. The ICF fraction for the present system is found to be least (for all v_{rel}) among the other four systems because of large negative α - Q value of ^{14}N . The α - Q values [$Q_\alpha(^9\text{Be}) = -2.648$ MeV, $Q_\alpha(^{16}\text{O}) = -7.16$ MeV; $Q_\alpha(^{12}\text{C}) = -7.37$ MeV; $Q_\alpha(^{13}\text{C}) = -10.64$ MeV; $Q_\alpha(^{14}\text{N}) = -11.62$ MeV] are different and therefore different amount of energy is required to separate out an α particle. Moreover, on the basis of α - Q value of the projectiles, one can also say that the projectile ^{14}N is most strongly bound and ^9Be is least tightly bound among the five projectiles. As such, as the projectile comes in the vicinity of the target nuclear field, it breaks up by releasing α particle which move in the forward direction, while the remaining part fuses with the target nucleus. It is evident from the Fig. 13 that percentage of ICF is more for the projectile with less negative α - Q value and ICF fraction decreases as the α - Q value becomes more and more negative. Hence, it is clear that in ICF reaction dynamics, α - Q value of the projectile is an important entrance channel parameter and may be considered to explain the behavior of ICF reactions at low energies.

It may be remarked that F_{ICF} data for an experiment on $^{11}\text{B} + ^{181}\text{Ta}$ system, since ^{11}B (α - Q value = -8.669 MeV) will lie on the right side of the ^{12}C bar shown in Fig. 13, and its $F_{ICF}(\%)$ value will also be less than $^{12}\text{C} + ^{181}\text{Ta}$ system and more than $^{13}\text{C} + ^{181}\text{Ta}$. Similarly, $^{14}\text{C} + ^{181}\text{Ta}$ system will have the least incomplete fusion fraction among these systems

as ^{14}C has an α - Q value of -12.0125 MeV. It is further emphasized that before reaching any conclusion on ICF reaction dynamics, more and more experimental data in this energy regime with non- α -cluster projectiles is required. This would help in developing a unified model for explaining ICF reaction dynamics.

IV. SUMMARY AND CONCLUSIONS

In the present work, the excitation functions of several radio-nuclides populated via CF and/or ICF processes, using a non- α -cluster beam ^{14}N on the target ^{181}Ta have been measured and analyzed within the framework of statistical model code PACE4 at energies ranging from $1.0145V_b$ to $1.3V_b$. The excitation functions of xn/pxn channels are found to be in good agreement with PACE4 predictions for the level density parameter $a = A/10$ MeV $^{-1}$, which indicates their production only via complete fusion process. However, the long tail in the excitation function of the residues ^{192}Hg , populated via $3n$ channel suggests the presence of precompound emission in this channel. Moreover, precursor contributions in pxn channels have also been observed and the independent cross sections of these channels have been deduced and are found to be in good agreement with the predictions of the code PACE4 for the same set of level density parameter ($a = A/10$). This indicates the production of these pxn channels solely via CF process. Further, in case of α -emitting channels, a significant enhancement in the experimental excitation functions as compared to the PACE4 predictions for the same set of parameters which were used for CF channels, has been observed. This enhancement is attributed to the contributions from ICF reactions. A strong dependence of F_{ICF} on normalized beam energy has been observed. The F_{ICF} is found to increase linearly with $Z_P Z_T$ both for α -cluster as well as non- α -cluster projectiles separately, indicating that the probability of breakup increases as Coulomb factor increases. The ICF strength function for projectiles, viz., ^9Be , ^{16}O , and $^{12,13}\text{C}$ (both α -cluster and non- α -cluster) on the same target ^{181}Ta has been compared with presently studied system $^{14}\text{N} + ^{181}\text{Ta}$, in terms of α - Q value of the projectiles for three different v_{rel} values ($v_{\text{rel}} = 0.045c, 0.053c, \text{ and } 0.056c$). It has been found that the contribution of ICF for ^{14}N is less as compared to the other α -cluster and non- α -cluster projectiles (^9Be , ^{16}O , and $^{12,13}\text{C}$) due to the more negative Q_α value of ^{14}N among all other projectiles. This behavior clearly reflects the projectile structure effect and shows how efficiently this parameter gov-

erns the ICF contribution. The F_{ICF} for the present system is found to be $\approx 5.5\%$ at $v_{rel} = 0.053c$, even though the projectile ^{14}N is much tightly bound ($Q_\alpha = -11.62$ MeV) as compared to other projectiles. As such, it is shown that the $\alpha - Q$ value well describes the ICF data. The break-up of α -cluster and non- α -cluster projectiles seem to follow the similar mechanism with relative ICF contribution depending on their Q_α value.

In order to achieve a better understanding and to have a more conclusive picture of ICF reaction dynamics, more experimental data for non- α -cluster projectiles especially ^{14}N covering a broader range of nuclei is required. Further, a comprehensive study of complimentary experiments, viz., recoil range distribution and particle- γ coincidence for the same

projectile-target combination is proposed to give a detailed insight of the ICF reaction dynamics. The new experimental data may help in the refinement of existing theoretical models and in developing universal systematics at energies $\approx 4-7$ MeV/nucleon.

ACKNOWLEDGMENTS

The authors thank the director of IUAC, New Delhi, India, and the chairperson of the Department of Physics, A. M. U, Aligarh (U.P), India, for providing all the necessary facilities to carry out this work. M.S.A. and B.P.S. thank the DST-SERB for providing financial support under Project No. CRG/2020/000136.

-
- [1] Yu. Ts. Oganessian *et al.*, *Nature (Lond.)* **400**, 242 (1999), and references therein.
- [2] S. Hofmann *et al.*, *Eur. Phys. J. A* **32**, 251 (2007); **14**, 147 (2002).
- [3] V. I. Zagrebaev, *Nucl. Phys. A* **734**, 164 (2004).
- [4] K. Siwek-Wilczynska, I. Skwira, and J. Wilczynski, *Phys. Rev. C* **72**, 034605 (2005).
- [5] R. Smolanczuk, *Phys. Rev. C* **59**, 2634 (1999).
- [6] E. Z. Buthelezi *et al.*, *Nucl. Phys. A* **734**, 553 (2004).
- [7] A. Diaz-Torres, D. J. Hinde, J. A. Tostevin, M. Dasgupta, and L. R. Gasques, *Phys. Rev. Lett.* **98**, 152701 (2007).
- [8] M. Dasgupta *et al.*, *Nucl. Phys. A* **787**, 144 (2007).
- [9] A. Yadav *et al.*, *Phys. Rev. C* **85**, 064617 (2012).
- [10] A. Diaz Torres and I. J. Thompson, *Phys. Rev. C* **65**, 024606 (2002).
- [11] A. Yadav *et al.*, *Phys. Rev. C* **96**, 044614 (2017) and references therein.
- [12] Mohd. Shuaib *et al.*, *J. Phys. G: Nucl. Part. Phys.* **44**, 105108 (2017).
- [13] H. C. Britt and A. R. Quinton, *Phys. Rev.* **124**, 877 (1961).
- [14] T. Inumura *et al.*, *Phys. Lett. B* **84**, 71 (1979); **68**, 51 (1977).
- [15] K. A. Geoffroy *et al.*, *Phys. Rev. Lett.* **43**, 1303 (1979).
- [16] C. Gerschel, *Nucl. Phys. A* **387**, 297 (1982).
- [17] P. P. Singh *et al.*, *Phys. Rev. C* **78**, 017602 (2008).
- [18] P. P. Singh *et al.*, *Phys. Lett. B* **671**, 20 (2009).
- [19] D. Singh *et al.*, *Phys. Rev. C* **81**, 027602 (2010).
- [20] T. Udagawa and T. Tamura, *Phys. Rev. Lett.* **45**, 1311 (1980).
- [21] R. Bass, *Nucl. Phys. A* **231**, 45 (1974).
- [22] J. Wilczynski *et al.*, *Nucl. Phys. A* **373**, 109 (1982).
- [23] M. Blann, *Phys. Lett.* **27**, 337 (1971).
- [24] J. P. Bondroff *et al.*, *Nucl. Phys. A* **333**, 285 (1980).
- [25] D. P. Singh *et al.*, *Phys. Rev. C* **81**, 054607 (2010).
- [26] M. K. Sharma, Unnati B. K. Sharma, B. P. Singh, H. D. Bhardwaj, R. Kumar, K. Golda, and R. Prasad, *Phys. Rev. C* **70**, 044606 (2004).
- [27] U. Gupta *et al.*, *Phys. Rev. C* **80**, 024613 (2009).
- [28] M. K. Sharma *et al.*, *Nucl. Phys. A* **776**, 83 (2006).
- [29] V. R. Sharma *et al.*, *Nucl. Phys. A* **946**, 182 (2016) and references therein.
- [30] Mohd. Shuaib *et al.*, *Phys. Rev. C* **94**, 014613 (2016).
- [31] A. Gavron, *Phys. Rev. C* **21**, 230 (1980).
- [32] Mohd. Shuaib *et al.*, *Phys. Rev. C* **99**, 024617 (2019) and references therein.
- [33] E. T. Subramaniam *et al.*, *Rev. Sci. Instr.* **77**, 096102 (2006).
- [34] E. Browne and R. B. Firestone, *Table of Radioactive Isotopes* (Wiley, New York, 1996).
- [35] J. K. Tuli, *Nuclear Wallet Card, National Nuclear Data Center* (Brookhaven National Laboratory, Upton, NY, 1995).
- [36] Mohd. Shuaib *et al.*, *Phys. Rev. C* **98**, 014605 (2018).
- [37] R. Prasad and B. P. Singh, *Fundamentals and Applications of Heavy Ion Collisions* (Cambridge University Press, Cambridge, UK, 2018).
- [38] U. Gupta *et al.*, *Nucl. Phys. A* **811**, 77 (2008), and references therein.
- [39] W. Hauser and H. Feshbach, *Phys. Rev.* **87**, 366 (1952).
- [40] M. Cavinato, E. Fabrici, E. Gadioli, E. GadioliErba, P. Vergani, M. Crippa, G. Colombo, I. Redaelli, and M. Ripamonti, *Phys. Rev. C* **52**, 2577 (1995).
- [41] R. D. Evans, *The Atomic Nucleus* (Tata McGraw-Hill, Bombay, 1995).
- [42] B. P. Singh, H. D. Bhardwaj, and R. Prasad, *Can. J. Phys.* **69**, 1376 (1991).
- [43] B. B. Kumar, A. Sharma, S. Mukherjee, S. Chakrabarty, P. K. Pujari, B. S. Tomar, A. Goswami, S. B. Manohar, and S. K. Datta, *Phys. Rev. C* **59**, 2923 (1999).
- [44] S. Mukherjee *et al.*, *Int. J. Mod. Phys. E* **15**, 237 (2006).
- [45] M. K. Sharma *et al.*, *J. Phys. Soc. Jpn.* **72**, 1917 (2003).
- [46] A. Yadav *et al.*, *Phys. Rev. C* **85**, 034614 (2012).
- [47] K. Kumar, T. Ahmad, S. Ali, I.A. Rizvi, A. Agarwal, R. Kumar, and A. K. Chaubey, *Phys. Rev. C* **89**, 054614 (2014).
- [48] S. Gupta, B. P. Singh, M. M. Musthafa, H. D. Bhardwaj, and R. Prasad, *Phys. Rev. C* **61**, 064613 (2000).
- [49] S. A. Tali *et al.*, *Nucl. Phys. A* **970**, 208 (2017).
- [50] P. P. Singh *et al.*, *J. Phys.: Conf. Ser.* **590**, 012031 (2015).
- [51] V. R. Sharma *et al.*, *Phys. Rev. C* **89**, 024608 (2014).
- [52] D. P. Singh, V. R. Sharma, A. Yadav, P. P. Singh, Unnati, M. K. Sharma, R. Kumar, B. P. Singh, and R. Prasad, *Phys. Rev. C* **89**, 024612 (2014).
- [53] H. Kumar *et al.*, *Nucl. Phys. A* **960**, 53 (2017).
- [54] K. Surendra Babu *et al.*, *J. Phys. G: Nucl. Part. Phys.* **29**, 1011 (2003).
- [55] K. Kumar, T. Ahmad, S. Ali, I.A. Rizvi, A. Agarwal, R. Kumar, K. S. Golda, and A. K. Chaubey, *Phys. Rev. C* **87**, 044608 (2013).
- [56] P. P. Singh, B. P. Singh, M. K. Sharma, Unnati, D. P. Singh, R. Prasad, R. Kumar, and K. S. Golda, *Phys. Rev. C* **77**, 014607 (2008).

- [57] H. Kumar *et al.*, *India J. Pure Appl. Phys.* **57**, 540 (2019).
- [58] D. P. Singh *et al.*, *Phys. Rev. C* **80**, 014601 (2009).
- [59] G. S. Li *et al.*, *Phys. Rev. C* **99**, 054617 (2019).
- [60] I. Majeed *et al.*, *Proceedings of the DAE Symposium on Nuclear Physics*, Vol. 64 (2019), <http://www.symppnp.org/proceedings/64/B6.pdf>.
- [61] M. K. Sharma *et al.*, *Eur. Phys. J. A* **31**, 43 (2007).
- [62] S. N. Ghoshal, *Phys. Rev.* **80**, 939 (1950).
- [63] M. K. Sharma *et al.*, *Phys. Rev. C* **94**, 044617 (2016).
- [64] M. K. Sharma *et al.*, *Phys. Rev. C* **91**, 014603 (2015).
- [65] D. P. Singh *et al.*, *EPJ Web Conf.* **86**, 00050 (2015).
- [66] P. P. Singh *et al.*, *Phys. Rev. C* **80**, 064603 (2009).
- [67] P. E. Hodgson, E. Gadioli, and E. Gadioli Erba, *Introductory Nuclear Physics* (Oxford University Press, New York, 2003).
- [68] H. Morgenstern, W. Bohne, W. Galster, K. Grabisch, and A. Kyanowski, *Phys. Rev. Lett.* **52**, 1104 (1984).